ACS APPLIED MATERIALS & INTERFACES

Research Article

www.acsami.org

One-Pot, Green, Rapid Synthesis of Flowerlike Gold Nanoparticles/Reduced Graphene Oxide Composite with Regenerated Silk Fibroin As Efficient Oxygen Reduction Electrocatalysts

Shengjie Xu, Liu Yong, and Peiyi Wu*

State Key Laboratory of Molecular Engineering of Polymer and Department of Macromolecular Science and Laboratory of Advanced Materials, Fudan University, Shanghai 200433, People's Republic of China

Supporting Information

ABSTRACT: Flowerlike gold nanoparticles (Au NPs)/reduced graphene oxide (RGO) composites were fabricated by a facile, one-pot, environmentally friendly method in the presence of regenerated silk fibroin (RSF). The influences of reaction time, temperature, and $HAuCl_4$: RGO ratio on the morphology of Au NPs loaded on RGO sheets were discussed and a tentative mechanism for the formation of flowerlike Au NPs/RGO composite was proposed. In addition, the flowerlike Au NPs/RGO composite showed superior catalytic performance for oxygen reduction reaction (ORR) to Au/RGO composites with other morphologies. Our work provides an alternative facile and green approach to synthesize functional metal/RGO composites.

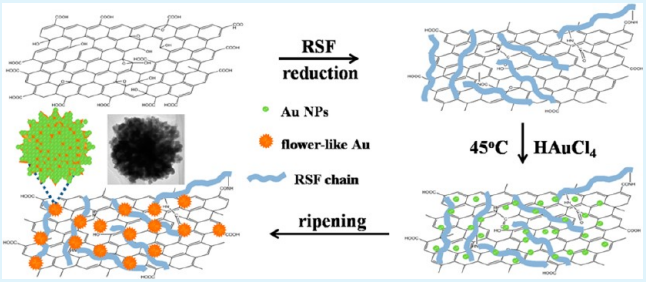

KEYWORDS: *flowerlike Au NPs, regenerated silk fibroin, graphene, electro-catalysis, oxygen reduction*

INTRODUCTION

Graphene is a kind of widely investigated and utilized nanomaterial in the past few years. The unique 2D single-layer C−C sp^2-bonded honeycomb structure gives it excellent mechanical, electrical, and thermal properties.[1−5] Besides, the high specific surface area makes it an ideal carrier for nanoparticles.[6−8] To date, there has been a great interest in functionalization and doping of graphene to manipulate its interfacial property and graft or load metal/metallic oxide nanoparticles.[9,10]

In general, most of graphenes are prepared by reducing graphene oxide (GO) by chemical,[6,11−15] electrochemical,[16] or hydrothermal[8,17] methods. Among them, the chemical reduction method is most widely employed. Reduced graphene oxide (RGO) prepared by traditional reducing agents has excellent electrical and thermal properties, but there exists several defects to limit the application of RGO in many areas: (1) the extensive adopted chemical routes to reduce GO usually use toxic agents such as sodium borohydride and hydrazine, and the residual agents are difficult to remove. (2) RGO sheets prepared by traditional chemical reduction method tend to aggregate and precipitate in water due to the strong $\pi-\pi$ stacking interaction. (3) It is not easy to decorate metal (or metal oxide) nanoparticles on RGO sheets due to limited active sites.

In recent years, researchers have found that some water-soluble polymers like PEG, PAA can obviously enhance the dispersibility of RGO in water.[18,19] However, among them, there are only a few polymers can efficiently reduce GO without adding other reducing agents. Comparing with these synthetic polymers, proteins are amphiphilic biomaterials with hydrophobic and hydrophilic segments in backbone or side groups, making them well-known for being "adhesive" to link hydrophobic and hydrophilic substrates.[20,21] Gao and co-workers prepared stable RGO suspension with lysozyme (lys) acting as the dispersant. They found that the suspension could be stably dispersed for more than six months and the dispersibility of lys-RGO solution was pH-sensitive.[46] Zheng found β-lactoglobulin could also efficiently disperse and decorate RGO.[22] Deng et al. fabricated well-dispersed RGO/metal composites in the presence of bovine serum albumin (BSA). BSA not only acted as the reducing agent and dispersant for RGO, but also provided active loading sites for metal NPs.[23,24] Besides, the cysteine,[25] tyrosine,[26,27] and glycine residues[28] have been investigated as mild and green reducing agents for metallic oxide and GO. It is reasonable that proteins containing these amino acid residues can be utilized as reducing agents. Nevertheless, there are only a few proteins being used for reducing and dispersing RGO, because many proteins are water-insoluble and much more expensive than synthetic polymers.

Regenerate silk fibroin (RSF) is a cheap, widely used, and water-soluble protein with 18 species of amino acid residues such as glycine, alanine, serine, and tyrosine,[29,30] which is

Received: September 21, 2012
Accepted: January 16, 2013
Published: January 16, 2013

prepared by destroying hydrogen bonds in silk fibroin and dissolving them in water. RSF can be easily and tightly absorbed onto RGO surfaces by $\pi-\pi$ stacking and H-bonding, while the $-COOH$ and $-NH_2$ groups on RSF chains can act as nucleation sites for metal NPs. So RSF can be a promising agent for the reduction and dispersion of RGO and in situ synthesizing RGO/metal NPs.

On the other hand, gold nanoparticles (Au NPs) are widely reported because of their specific optical, catalytic, electric and delivery properties.[31−35] The uniform nanostructures with various morphologies have been fabricated, such as spheres,[6,36,37] plates,[38] wires,[39] cubes,[34,40,41] dendrites,[42−44] and flowers.[45,46] Plenty of reports have also been devoted to the fabrication of Au NPs/RGO composite. Huang et al. fabricated Au/RGO composites via sonochemical reduction with the assistance of hydrazine and SDS, and the composites were further applied to the electrical detection of DNA hybridization.[47] Our group also successfully prepared well-dispersed Au/RGO composites by using sodium citrate as the reducing agent.[6] Besides, hydrothermal method was also widely employed to prepare metal (or metal oxide)/RGO composites.[48,49] However, Au NPs prepared in their works were usually disorderly distributed with irregular shapes and different sizes. Moreover, Au/RGO composites have been gotten much more interest during the past few years because of their superior performance in many areas, such as surface-enhanced Raman scattering,[6] biosensors,[47] and catalysis.[50] Recently, metal (metallic oxide)/RGO[51−53] or heteroatom doped RGO[54−56] were reported to have remarkable effects on electro-catalysis toward oxygen reduction reaction (ORR). They are much cheaper than the commercial ORR catalyst Pt/C; however, the preparation of those composites is always very complicated or harsh. So a facilely prepared, efficient, and green catalyst is urgently needed for ORR.

Here, we present a facile, green, and rapid approach to synthesize uniformly distributed flowerlike Au NPs/RGO composite using RSF as both a reducing agent for GO and chloroauric acid and an "adhesive" for binding Au NPs and RGO sheets. The Au NPs/RGO composites could be easily and stably redispersed in water after washing for several times due to the amphiphilicity of RSF chains absorbed on RGO sheets. Furthermore, the flowerlike Au NPs/RGO composite exhibits better catalytic activity toward ORR than other Au NPs/RGO composites, making it a promising catalyst in electrochemistry.

EXPERIMENTAL SECTION

Materials. Chloroaunic acid tetrahydrate ($HAuCl_4{\cdot}4H_2O$) was purchased from Sinopharm Chemical Reagent Co. Ltd. Graphite powder (8000 meshes, 99.95%) was obtained from Aladdin Reagent Co. Ltd. All other reagents are of analytical grade and used without further purification.

Preparation of RSF Aqueous Solution. RSF aqueous solution was prepared as described elsewhere.[57] Briefly, cocoons of *Bombyx mori* was boiled for 45 min in an aqueous solution of 5 W/V% Na_2CO_3 to remove silk sericin and wax. The extracted silk fibroin was dissolved into a 9.3 M LiBr solution at 40 °C for 1 h. The solution was then dialyzed in deionized water using a Slide-a-Lyzer dialysis cassette (molecular weight cutoff, MWCO, 14000) for three days. Then the dialyzed silk fibroin solution was centrifuged at 6000 rpm for about 5 min to remove insoluble impurities. The final concentration of the silk fibroin aqueous solution was ca. 3−4 wt %.

Preparation of GO. GO was prepared by the modified Hummers method.[58] In brief, 5 g of expandable graphite powders and 2.5 g of potassium nitrate were mixed in 115 mL of concentrated sulfuric acid at 0 °C with ice−water bath. Then 15 g of potassium permanganate was added under vigorous stirring. After increasing the temperature to 35 °C, 115 mL of water was added to the mixture rapidly before keeping the temperature under 100 °C for 30 min. Then another 700 mL of water was added, followed by adding 50 mL of H_2O_2 (30 wt %). Finally, the resulting suspension was filtered and dialyzed for 2 weeks to remove the remaining metal ions, and then freeze-dried before use.

Preparation of Au NPs/RGO Composites. Typically, 16 mg of GO was sonicated and dispersed in 8 mL of water, then 10 mL RSF solution (3 wt %) was added, followed by raising pH to around 12 by the addition of 1.0 M NaOH. The mixture was sonicated for another 30 min, and then heated to 50−70 °C for 3−6 h. After the yellow-brown solution of GO gradually turned black, 14.4 mL of $HAuCl_4$ (25 mM) was added before adjusting pH to 7 by 1.0 M HCl, and then heating to 45 °C for 5 min. The solution was cooled rapidly and then excessive RSF and smaller Au NPs that were not absorbed on graphene were removed by a 30 min centrifugation at 12 000 rpm for several times. The resulting black precipitates were dried or redispersed in water for further characterization.

Electrochemical Measurement. *1. Cyclic Voltammetry (CV).* CV was performed with a computer-controlled potentiostat (CHI660D) in a standard three-electrode cell using saturated calomel electrode as the reference electrode, a platinum wire as the counter electrode and a glassy carbon electrode as the working electrode. The working electrode was prepared as reported previously.[55] In brief, 5 mg of catalyst was dispersed in 3 mL of isopropanol by 45 min sonication to form homogeneous suspension. Then 5 μL of suspension was dropped onto a glassy carbon electrode with 5 mm diameter, and 5 μL of Nafion solution (5 wt %) was coated after the suspensions was dried. The three electrodes were put into 0.1 M KOH solution. A flow of O_2 or N_2 was maintained for 40 min to achieve O_2-saturated or O_2-free. The working electrode was cycled at least 5 times in the potential range from −0.8 to 0.2 V at a scanning rate of 5 mV/s.

2. Rotating Disk Electrode (RDE) Measurement. The working electrode was prepared by the same method as CV. The measurements were performed at a scanning rate of 5 mV/s with different rotating speeds from 100 to 1300 rpm. Koutecky−Levich plots (J^{-1} vs $\omega^{-1/2}$) were analyzed at various electrode potentials to determine the number of electrons involved in oxygen reduction. The current density J is related to the angular velocity ω according to

$$\frac{1}{J} = \frac{1}{J_L} + \frac{1}{J_K} = \frac{1}{B\omega^{1/2}} + \frac{1}{J_K}$$

$$B = 0.62nFC_{O_2}D_2^{2/3}\nu^{-1/6}$$

Where J_k and J_L are the kinetic and diffusion-limiting current densities; n is the number of electrons transferred in reduction; ω is the angular velocity; F is Faraday constant; C_{O_2} is concentration of O_2 in solution; D_{O_2} is the diffusion coefficient of O_2 in solution; and ν is the kinematic viscosity for KOH.

Characterization. The transmission electron microscope (TEM) images of Au NPs/RGO were taken on microgrid carbon film (T11012) with a JEOL JEM2011 at 200 KV equipped with selective area electron diffraction (SAED). Scanning electron microscope (SEM) observations were performed on Hitachi-S-4800 FE-SEM with gold coating. To evaluate the dispersion state of the GO sheets in the suspensions, we obtained atomic force microscopy (AFM) images using a Multimode Nano4 in the tapping mode. X-ray diffraction (XRD) patterns were acquired by a D8 ADVANCE and DAVINCI.DESIGN (Bruker) X'pert diffractometer with Cu K_α radiation. UV−vis spectra were measured on a Hitachi U-2910 spectrophotometer. Raman spectra were recorded on a Renishaw inVia Reflex micro-Raman spectrometer with He/Ne laser excitation at 632.8 nm. Thermo gravimetric analysis (TGA) was carried out at a heating rate of 20 °C/min on Perkin-Elmer Pyris-1 TGA in nitrogen at a flow rate of 40 cm^3/min. Fourier transform infrared (FTIR) spectra were recorded on a Nicolet Nexus 470 spectrometer.

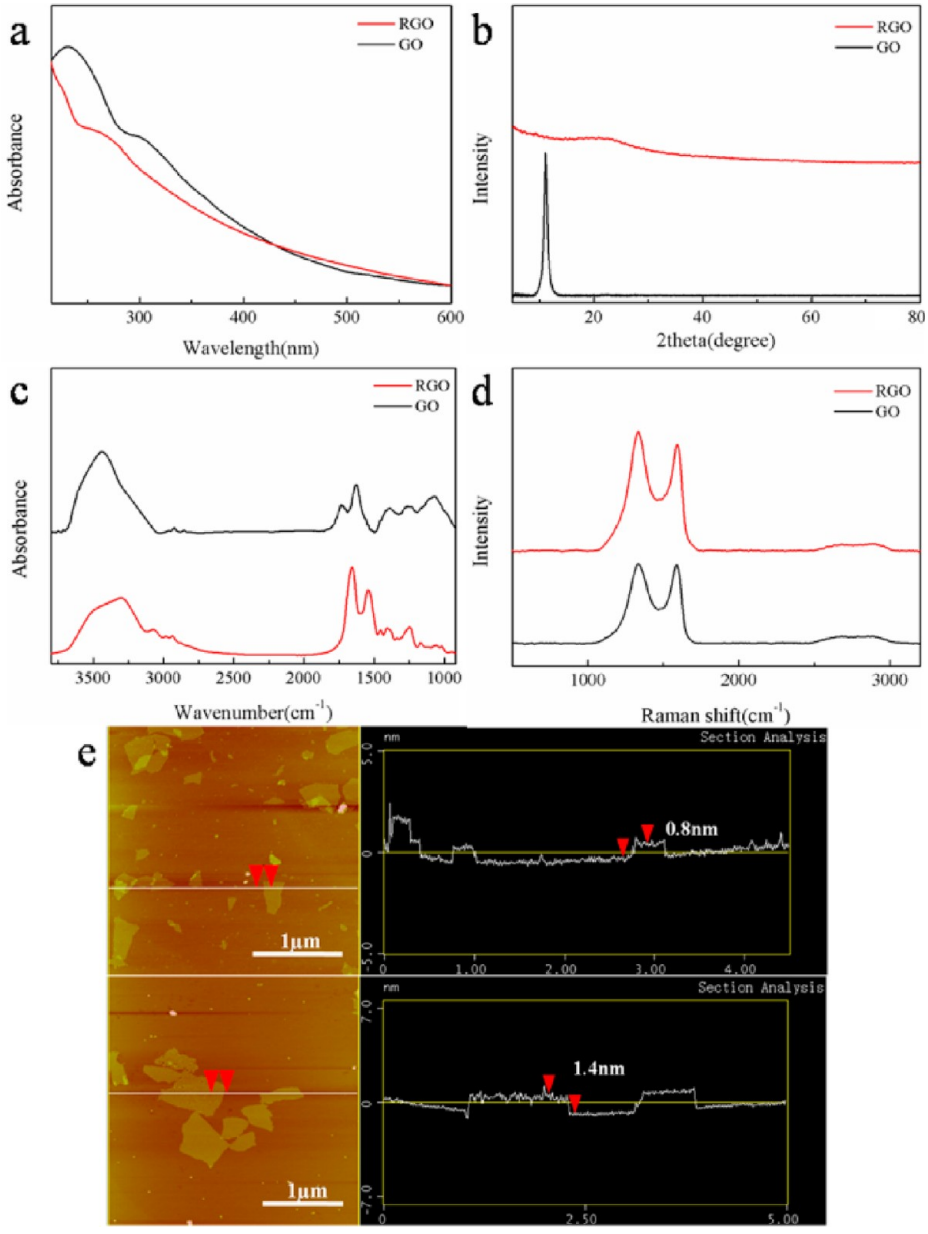

Figure 1. (a) UV−vis spectra, (b) XRD patterns, (c) FTIR spectra, (d) Raman spectra of GO and RGO reduced by RSF. (e) AFM images of GO (top) and RGO (bottom).

RESULTS AND DISCUSSION

RGO was prepared by heating the mixture of GO and RSF at 60 °C for 4 h. To prove GO was successfully reduced, several characterizations were utilized after the products were washed for several times. Figure 1a shows the UV−vis spectra of GO and RSF reduced RGO. The peaks around 230 and 305 nm could be ascribed to $\pi-\pi^*$ transition and $n-\pi^*$ transition absorption of GO. After reduction, the peak around 230 nm red shifts to 265 nm and the peak at 305 nm disappears, indicating GO was well reduced to RGO with highly electronic conjugated structure by RSF.[6,59]

XRD patterns also reveal that GO was almost completely reduced by RSF (Figure 1b). As reported previously, the peak at $2\theta = 11.5°$, corresponding to an average interlayer spacing of ~9 Å, is assigned to the characteristic peak of GO. While for the RGO sample, the peak at $2\theta = 11.5°$ disappears, replaced by a broad peak at $2\theta = 23.5°$, which is probably assigned to RGO characteristic peak. The interlayer spacing is about 3.9 Å, which is a little larger than that of RGO reduced by other reducing agents (3.6 Å).[8] The main reason is that many RSF chains intercalated in graphene sheets by H-bonding, $\pi-\pi$ stacking and covalent bonds during GO reduction. AFM images also demonstrate that RSF chains adhere to RGO sheets after reduction, as shown in Figure 1e. The thickness of GO is about 0.8 nm, which is consistent with the previous report,[9] indicating they are monolayered and well-dispersed. Theoretically, the thickness of GO sheet should decrease after reduction; however, in our experiment the height increases to 1.4 nm, which is much thicker than pristine graphene.[60] Besides, the surface of such RGO is rougher than that of initial GO. Both results suggest that RSF chains are tightly absorbed on RGO sheets, and the thickness of RSF is about 0.4 nm (both sides of RGO could absorb RSF chains). The anchored RSF chains can

dx.doi.org/10.1021/am302076x | ACS Appl. Mater. Interfaces 2013, 5, 654−662

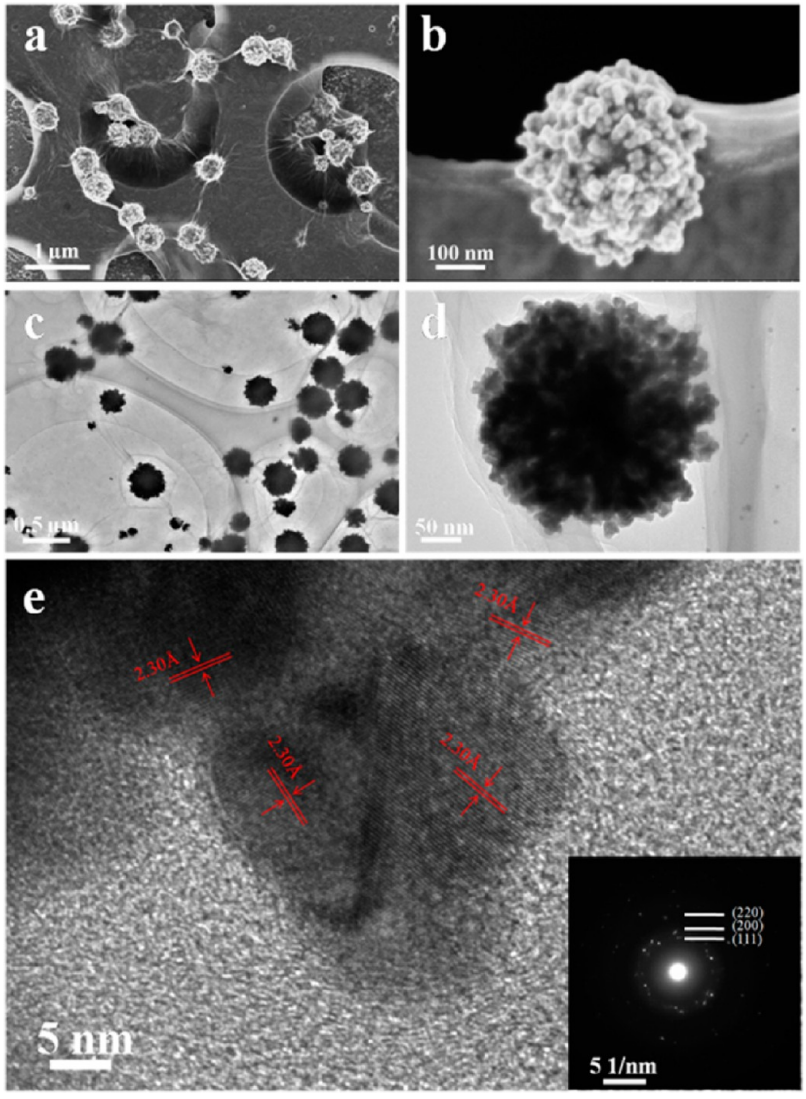

Figure 2. EM images of flowerlike Au NPs loaded on RGO sheets. (a, b) SEM of Au NPs at a reaction time of 5 min, (c, d) TEM and (e) HR-TEM of Au NPs at a reaction time of 5 min. The lattice spacing of 2.30 Å can be indexed as the (111) face of Au. The inset of e is the SAED pattern of flowerlike Au NPs.

also account for the good dispersibility of RGO sheets in water after centrifugation and washing for several times.

Another potent evidence for GO reduction is FTIR. The characteristic peaks of GO at 3420, 1720, 1395, 1240, and 1060 cm^{-1} are ascribed to O−H stretching, C═O stretching of COOH, O−H deformation, C−OH stretching, and C−O stretching, respectively. After reduction, the C═O stretching band disappears and the peaks of other oxygenic functional groups in relation to GO strongly decrease. In FTIR spectrum of RGO, the peaks at 3270, 3060, 1650, and 1540 cm^{-1} are assigned to N−H stretching, C−H stretching in aromatic rings, amide I, and amide II, respectively. Because both the aromatic ring and peptide bonds exist in RSF chains, it also demonstrates that some RSF chains are anchored on RGO sheets during the reduction process.

Raman spectroscopy is regarded as a powerful technique to characterize graphitic derivatives. As we know, there are two characteristic peaks in the spectrum of raw graphite, the D band at 1330 cm^{-1} assigned to the disorder carbon, defects, and edges on graphitic derivative plane, and the G band at 1582 cm^{-1} arising from the Brillouin zone center E_{2g} mode, corresponding to ordered sp^2-bonded carbon. Figure 1d shows the Raman spectra of GO and RGO. For GO sample, the D band slightly shifts to 1335 cm^{-1} and the G band shifts to 1591 cm^{-1} comparing with graphite, indicating a decrease in the size of the in-plane sp^2 structure due to the oxidation and exfoliation process of graphite. The two bands between 2600 to 2950 cm^{-1} are assigned to 2D and D+G band, respectively.[13] whereas for RGO, the G band further blue shifts to 1594 cm^{-1} with the D band almost unchanged. The intensity ratio of D/G increases from 1.03 to 1.17, suggesting a further decrease of the size of the sp^2 domains during the reduction of GO.

The flowerlike Au NPs/RGO composite was prepared by mixing $HAuCl_4$ solution (25 mM) and as-prepared RGO solution (ca. 1 g/L) with the ratio 4:5 (V:V), then reacting at 45 °C for 5 min. Figure 2a shows the SEM image of flowerlike Au NPs/RGO composite, the Au NPs are almost monodispersed in a size of 200−300 nm with rough surfaces. The wrinkles around Au NPs on the microgrid carbon film indicate crumpling and folding of RGO during the drying process. Enlarged image (Figure 2b) indicates these Au NPs are flowerlike and composed of a number of 10 nm nanoparticles.

dx.doi.org/10.1021/am302076x | ACS Appl. Mater. Interfaces 2013, 5, 654−662

The FTIR spectrum of flowerlike Au NPs/RGO composite is almost the same to RSF reduced RGO (see Figure S1a in the Supporting Information), and there is still a obvious weight loss of RSF in the TGA curve of flowerlike Au NPs/RGO composite (see Figure S1b in the Supporting Information), indicating that RSF chains are still tightly absorbed on RGO sheets after the formation of Au NPs. It reveals the RSF chains probably not only act as a reducing agent for GO and chloroauric acid, but also serve as an "adhesive" for binding RGO and Au NPs. From the TEM image (Figure 2c), we can observe some flowerlike Au NPs on RGO sheets which cover the holes of microgrid carbon film. Enlarged image clearly shows the edge of RGO sheets under Au NPs (Figure 2d). Moreover, these Au NPs are not stacked very densely, so the specific surface area of the flowerlike Au NPs should be much higher than spherical NPs with the same size, resulting in the potential application in catalysis. The HR-TEM image reveals all the lattice spacings in the four different crystalline areas are 2.30 Å (Figure 2e), which is consistent with other reports, indexing as the (111) face of Au.[25,43] Selected-area electron diffraction (SAED) exhibits a mixed diffraction pattern, including (111), (200), and (220) faces, which is in accordance with the XRD pattern (see Figure S2 in the Supporting Information), suggesting the presence of defects and multiple crystal domains in Au crystals.[44]

Effect of Time and Temperature on the Morphology and Optical Property of Au NPs. To investigate the growth process of the flowerlike Au NPs, we performed time-resolved experiments for the sample with the ratio of $HAuCl_4$:RGO about 4:5(V:V), and TEM observations were utilized to monitor the morphology changes during the experiments. Figure 3a shows the products obtained after 3 min. Although the reaction time is very short, there are already many Au NPs loaded on RGO planes, suggesting the fast formation of Au in the presence of RSF. Plenty of nanoparticles with a size of 10 nm aggregated to form loose and irregularly ordered Au particles, whereas the others are scattered on RGO plane. At 5 min, monodispersed flowerlike Au NPs are formed with a size of 300 nm, along with drastic decreasing of scattered single Au nanoparticles (Figure 3b), indicating that the large flowerlike Au NPs are formed by consuming smaller Au nanoparticles in a Ostwald repining process.[61] The 10 nm nanoparticles can be hardly found when reaction time increased to 10 min; meanwhile, the aggregated particle further increased to 400 nm along with the surface becoming rougher than that at 5 min (Figure 3c), which is consistent with our assumption. When the reaction time is prolonged to 20 min, the flowerlike Au NPs disappear, replaced by larger clusters which are also composed of a mass of nanoparticles (Figure 3d). It seems that the flowerlike Au NPs are not very stable and tend to collapse with much more Au reducing and aggregating.

Temperature is another important factor for regulating the morphology of Au NPs. Figure 3e shows the TEM image of products prepared at 37 °C after 30 min reaction, some small particles are formed with an irregular shape. With decreasing temperature to room temperature (about 25 °C), spherical Au NPs (15 nm) are uniformly distributed on RGO planes. Generally, for a kinetically controlled reaction, elevating temperature or prolonging reaction time would lead to the same results. However, in our system, the morphologies of Au NPs obtained at a higher temperature and a longer time are totally different, indicating the formation of flowerlike Au NPs is a thermodynamic process and in which temperature acts as a crucial role.

Previous researches have reported Au NPs with different morphologies or sizes would present distinct optical properties.[34,41] UV−vis spectroscopy was employed to detect optical absorption of Au NPs prepared after different reaction time. As shown in Figure 4, the 15 nm spherical Au NPs prepared at room temperature have a typical peak at 528 nm (Figure 4f), which is consistent with other reports.[62,63] When the temperature is increased to 37 °C, the peak red shifts to 538 nm (Figure 4e) with the size and roughness of Au particles increasing (Figure 3e). When the reaction temperature is 45 °C, the perfect flowerlike Au NPs have a broad band ranged from 500 to 850 nm (Figure 4b, c) with the main peak red shifting to 645 nm. For the irregular (Figure 4a) and collapsed (Figure 4d) Au NPs, despite of the presence of secondary tips,

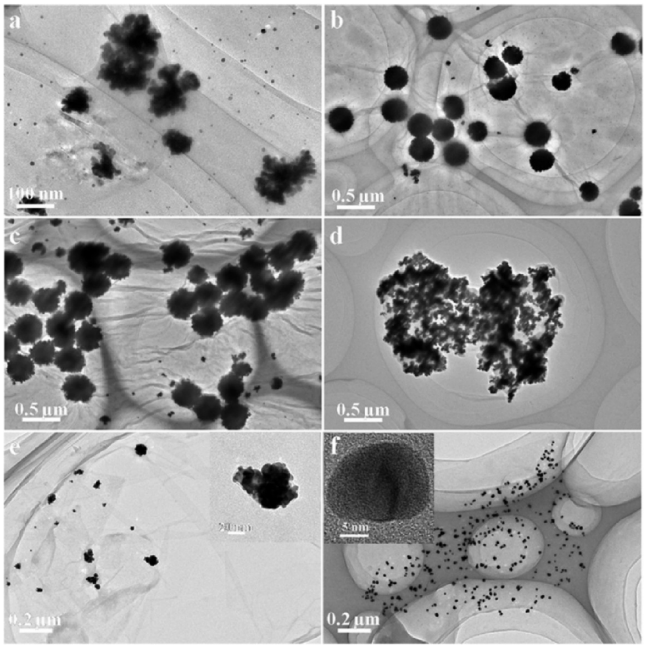

Figure 3. TEM images of Au NPs/RGO composites at different reaction time. (a) 3 min at 45 °C, (b) 5 min at 45 °C, (c) 10 min at 45 °C, (d) 20 min at 45 °C, (e) 30 min at 37 °C, (f) 60 min at room temperature. The insets of e and f are the enlarged images of each sample.

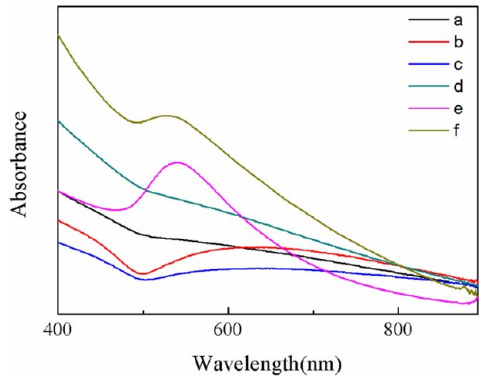

Figure 4. UV−vis spectra of the synthesized Au NPs at different reaction time: (a) 3 min at 45 °C, (b) 5 min at 45 °C, (c) 10 min at 45 °C, (d) 20 min at 45 °C, (e) 30 min at 37 °C, (f) 60 min at room temperature.

they do not present an obvious absorption peak, which might be caused by the irregularly stacking structure of Au NPs (Figure 3a, d). The above results suggest that the optical properties are not only dependent on the secondary tips of the particle, but also related with the aggregated structure of Au NPs.

Effect of the Initial Ratio of $HAuCl_4$: RGO on the Morphology of Au NPs. Figure 5 shows the TEM images of Au NPs/RGO composites prepared with different ratios of $HAuCl_4$: RGO. It indicates that the ratio of $HAuCl_4$: RGO is very crucial for fabricating flowerlike Au NPs, which could only be prepared with the ratio about 4:5. When the added $HAuCl_4$ is halved, particles are incomplete with some defects existing on the surface (Figure 5a). Although the particles are nearly monodispersed and stacked by a large amount of nanoparticles, they are much smaller than flowerlike particles. It seems that these particles are the intermediate phase of the flowerlike Au NPs and in this case the Au nanoparticles are not enough to form complete flowerlike morphology. When the amount of $HAuCl_4$ is doubled, the Au NPs collapse to form dendritic clusters (Figure 5b, d). We find that the branches are also made up of several nanoparticles in the enlarged image (Figure 5c).[64] It seems that the number of branches on the Au particle surface determines the optical property of Au particle (see Figure S3 in the Supporting Information); that is, the main peak in UV−vis spectra would red shift when the branches increase. Both the lattice spacings of these two Au NPs are 2.3 Å in HR-TEM images (Figure 5c), which is consistent with flowerlike Au NPs, indicating that the crystal phase is invariant with changing initial ratio of $HAuCl_4$: RGO.

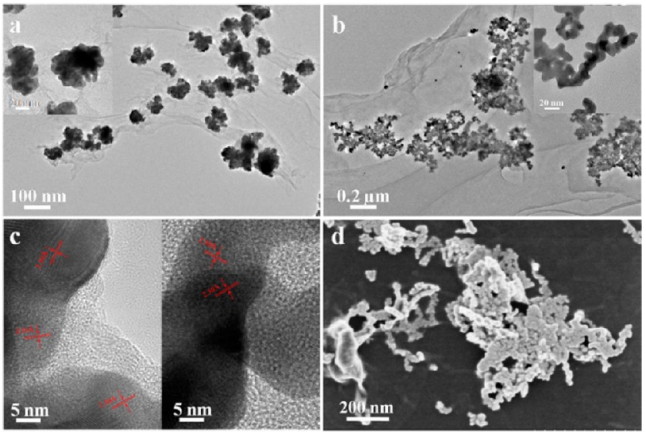

Figure 5. TEM images of Au NPs/RGO composites prepared with different ratios of $HAuCl_4$: RGO, (a) 2:5, (b) 8:5 (V:V). (c) Corresponding HR-TEM images of a (left) and b (right); the lattice spacing is 2.30 Å. (d) SEM image of Au NPs/RGO composite with the ratio of $HAuCl_4$:RGO = 8:5. The concentrations of $HAuCl_4$ and RGO in this system are 25 mM and 1 g/L.

Probable Formation Mechanism for the Flowerlike Au NPs on RGO Sheets. Based on the above results, a possible mechanism for the formation of flowerlike Au/RGO composite in the presence of RSF chains was proposed, as depicted in Figure 6. First, GO was reduced by cysteine, tyrosine, and glycine residues on RSF chains. During the reduction process, some RSF chains intercalated in RGO sheets and acted as a dispersing agent for RGO. There were three mutual interactions between RGO sheets and RSF chains, e.g., amide bonds (covalent interactions), H-bonds and $\pi-\pi$ interactions between the conjugated structures of RGO and the aromatic moieties of tyrosine or tryptophane (noncovalent interactions).[29,65] After GO reduction, $HAuCl_4$ was added before adjusting solution pH to 7, because alkaline condition was not favorable to flowerlike Au NPs formation in our experiment. The Au crystals nucleated rapidly in vicinity of -NH_2 groups due to the electrostatic interaction, followed by a fast formation of complex structures. From Figure 3a−c, the number of scattered nanoparticles significantly decreases along with Au crystal growth, suggesting that the final flowerlike Au NPs were formed through the consumption of smaller spherical nanoparticles.[44,45] The main driving force for this process was the reduction of surface energy. Besides, and RSF chains acted as the stabilizer for these particles. In early time, the nanoparticles were formed rapidly, which would spontaneously aggregate to

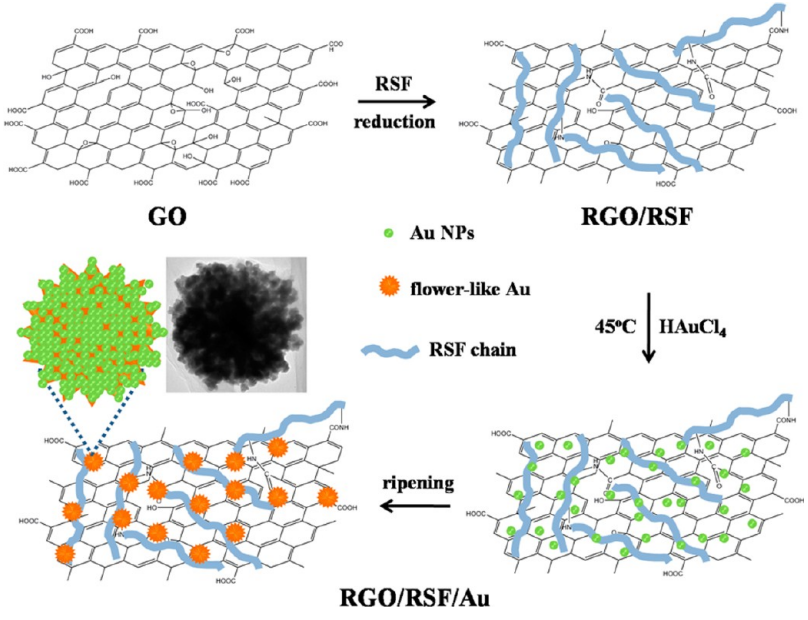

Figure 6. Schematic illustration of the procedure for the synthesis of flowerlike Au/RGO composite.

dx.doi.org/10.1021/am302076x | ACS Appl. Mater. Interfaces 2013, 5, 654−662

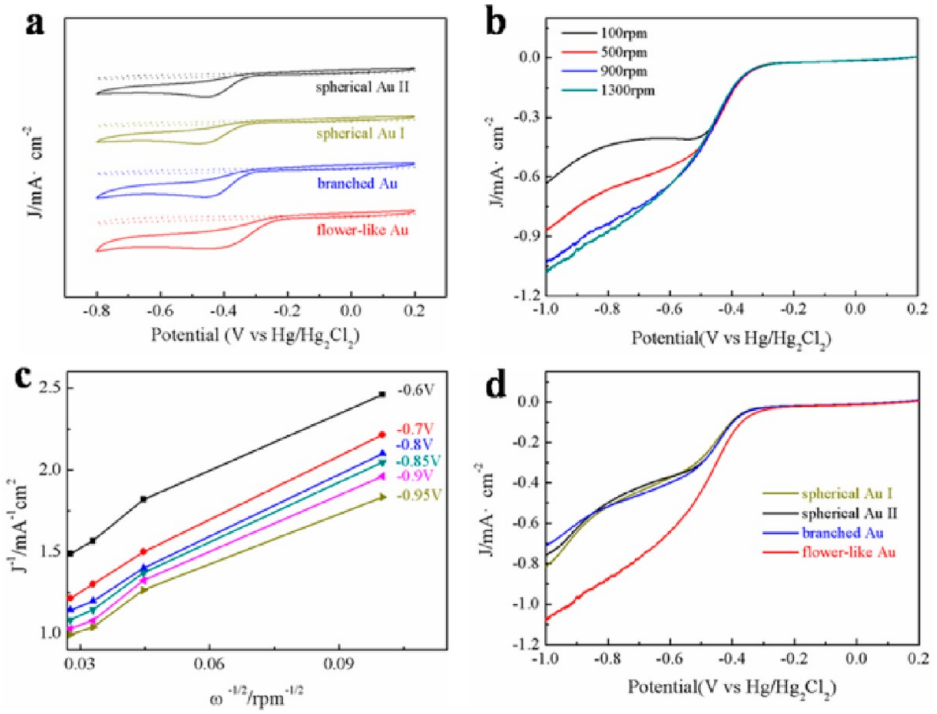

Figure 7. (a) CV curves of flowerlike Au NPs/RGO composite, branched Au NPs/RGO composite, spherical Au (I, II) NPs/RGO composite. (b) RDE curves of flowerlike Au NPs/RGO composite in O_2-satureated 0.1 M KOH solution with different rotation speeds. (c) The Koutecky–Levich plots of flowerlike Au NPs/RGO composite derived from the RDE measurements. (d) RDE curves of flowerlike Au NPs/RGO composite, branched Au NPs/RGO composite, spherical Au (I, II) NPs/RGO composite in O_2-satureated 0.1 M KOH solution at a rotation speed of 1300 rpm.

from irregular particles. Due to the minimization of surface energy, the particles would gradually tend to form larger spheres. With prolonging the reaction time, the rate of Au formation decreased and the growth of Au became diffusion-controlled due to the depletion of $HAuCl_4$, so the nanoparticles would stack in favorable directions. Some tips on the surface that could reduce the nucleation energy more easily accepted adatom attachment, resulting in the anisotropic growth of Au particles. Subsequently, branches would protrude from the surface of the spherical particles, and form the observed flowerlike structures.[45]

Electrocatalysis Application of Flowerlike Au NPs/RGO. The electrocatalysis activity of flowerlike Au NPs/RGO composite for ORR was first characterized by cyclic voltammetry (CV) in 0.1 M KOH on a glassy carbon electrode. As shown in Figure 7a, the onset potential and peak potential of flowerlike Au NPs/RGO composite are −0.22 V and −0.40 V against saturated calomel electrode, respectively, which are ∼60 mV more positive than RGO sheets (see Figure S4 in the Supporting Information).[56,66] Catalytic property of flowerlike Au NPs/RGO composite was compared with other three Au NPs with different shapes: branched, spherical I, and spherical II. Branched Au NPs are composed of several separate ∼10 nm nanoparticles[67] (see Figure S5c in the Supporting Information). The difference between two spherical Au NPs is the particle size, where, the diameter of I is about 10 nm (see Figure S5a in the Supporting Information) and II about 80 nm (see Figure S5b in the Supporting Information). Although the branched Au NPs/RGO composite also has sharp edges or tips, the onset potential is ∼80 mV more negative than that of flowerlike Au NPs/RGO, and the peak potential is ∼30 mV, indicating that the aggregation structure have a crucial effect on the catalytic ability of Au NPs. For flowerlike Au NPs/RGO composite, the loosely stacked structures not only maintain the high specific surface area of the single nanoparticles, but also provide many secondary tips which could act as active reaction sites for ORR, so the catalysis activity is better than other Au NPs/RGO composites. Generally, the oxygen in solution would be reduced at these secondary tips and produce electrons, because of the excellent electrical conductivity of Au and RGO sheets. The electrons would be quickly captured by Au particle, and then efficiently transferred to RGO sheets, whereas for the branched Au NPs, the Au NPs are so dispersive that the produced electron may be quenched in the transmission process, which would greatly affect the catalytic efficiency. The potential of spherical I and spherical II Au NPs/RGO composites are almost the same and further more negative than that of flowerlike Au NPs/RGO (onset potential of −0.33 V and peak potential of −0.46 V, against saturated calomel electrode). The most probable reason is that both the two Au NPs do not have secondary branches or sharp tips, resulting in lower specific surface area and much less reaction sites than flowerlike Au NPs.

We further investigated the influence of Au content in the composite on the catalytic property for ORR. EDS was employed to measure Au contents, as shown in Figure S5 in the Supporting Information. Although the mass fraction in branched Au (22.42 wt %) is much bigger than others, the catalytic performance of branched Au NPs/RGO composite is much lower than flowerlike Au NPs/RGO composite, suggesting that Au content has little effect on the catalytic property of Au. Analogously, the crystal phases of these four Au NPs are all the same, excluding the influence of crystal phase on the catalytic ability toward ORR (see Figure S2 in the Supporting Information).

dx.doi.org/10.1021/am302076x | ACS Appl. Mater. Interfaces 2013, 5, 654−662

The ORR catalytic activity of the above catalysts was also measured by linear-sweep voltammetry (LSV) in O_2-saturated 0.1 M KOH solution on rotating disk electrode. Figure 7b shows the LSV curves of flowerlike Au NPs/RGO composite with different electrode rotation rates. The measured current density shows typical increase with increasing rotation rate due to the enhanced diffusion of electrolytes, indicating the diffusion rate is a key factor for the catalytic process. The Koutecky–Levich equation is employed to calculate the transferred electron number per O_2 molecule involved in the ORR process, and the corresponding curves are plotted for different potentials in Figure 7c. The nearly parallel and straight fitting lines indicate that the reduction reaction of dissolved O_2 is a first-order reaction.[55,68,69] The *n* value for flowerlike Au NPs/RGO composite is also calculated to be about 3.44–4.07 V over the potential ranged from −0.95 V to −0.6 V (see Figure S6 in the Supporting Information), suggesting a direct four-electron transfer pathway for producing OH^- ion toward the flowerlike Au NPs/RGO catalyzed ORR process.

Additionally, the LSV curves for different catalysts in O_2-saturated 0.1 M KOH solution at a rotation rate of 1300 rpm are shown in Figure 6d. Notably, the flowerlike Au NPs/RGO composite exhibits much bigger current density, and the onset potential is ∼40 mV more positive than other composites, revealing that the catalytic ability of flowerlike Au NPs/RGO composite is much more outstanding and the flowerlike Au NPs/RGO composite is able to be an excellent catalyst for ORR.

CONCLUSION

In summary, we synthesized a flowerlike Au NPs/RGO composite in a facile and green approach in the presence of RSF. RSF not only acted as a reducing agent for GO and chloroauric acid, but also served as an "adhesive" for binding Au NPs and RGO. The prepared composite could be easily and stably redispersed in water because of the amphiphilicity of RSF chains. By changing reaction parameters like reaction time, temperature, and pH, the size, shape, and crystal aggregation of the Au NPs loaded on RGO can be regulated. The electrochemical experiments show that the catalytic ability of flowerlike Au NPs/RGO composite toward ORR is more excellent than other Au/RGO composites. It might be a new efficient catalyst in electrochemistry area. Moreover, the absorption throughout the visible and near-infrared region in UV–vis spectra makes it have potential applications in biological and colorimetric sensing area. In addition, our work probably provides an alternative approach to expediently prepare functional metal/RGO composites.

ASSOCIATED CONTENT

Supporting Information

Description related to synthesis of spherical and branched Au NPs/RGO composites, typical FTIR spectra (Figure S1a) and TGA curves (Figure S1b) of reduced RGO and as-fabricated flowerlike Au NPs/RGO composite, XRD patterns (Figure S2) and UV–vis spectra (Figure S3) of different morphologies Au NPs/RGO composites, CV curve of RSF reduced RGO (Figure S4), TEM and EDS of different morphologies Au NPs/RGO composites (Figure S5), and dependence of *n* value of flowerlike Au NPs/RGO composites on different potential (Figure S6). This material is available free of charge via the Internet at http://pubs.acs.org/.

AUTHOR INFORMATION

Corresponding Author

*E-mail:peiyiwu@fudan.edu.cn. Tel.: +86-21-65643255. Fax: +86-21-65640293.

Notes

The authors declare no competing financial interest.

ACKNOWLEDGMENTS

This work was financially supported by the National Science Foundation of China (NSFC) (20934002, 51073043) and the National Basic Research Program of China (No.2009CB930000). We gratefully acknowledge the great help from the group of Professor Aishui Yu.

REFERENCES

(1) Schedin, F.; Geim, A. K.; Morozov, S. V.; Hill, E. W.; Blake, P.; Katsnelson, M. I.; Novoselov, K. S. *Nat. Mater.* **2007**, *6*, 652–655.
(2) Tsoukleri, G.; Parthenios, J.; Papagelis, K.; Jalil, R.; Ferrari, A. C.; Geim, A. K.; Novoselov, K. S.; Galiotis, C. *Small* **2009**, *5*, 2397–2402.
(3) Geim, A. K. *Science* **2009**, *324*, 1530–1534.
(4) Wu, J. H.; Tang, Q. W.; Sun, H.; Lin, J. M.; Ao, H. Y.; Huang, M. L.; Huang, Y. F. *Langmuir* **2008**, *24*, 4800–4805.
(5) Sun, Y. Q.; Wu, Q. O.; Shi, G. Q. *Energy Environ.. Sci.* **2011**, *4*, 1113–1132.
(6) Sun, S. T.; Wu, P. Y. *Phys. Chem. Chem. Phys.* **2011**, *13*, 21116–21120.
(7) Wu, S.; Yin, Z.; He, Q.; Lu, G.; Zhou, X.; Zhang, H. *J. Mater. Chem.* **2011**, *21*, 3467–3470.
(8) Shen, J.; Yan, B.; Shi, M.; Ma, H.; Li, N.; Ye, M. *J. Mater. Chem.* **2011**, *21*, 3415–3421.
(9) Shen, J. F.; Long, Y.; Li, T.; Shi, M.; Li, N.; Ye, M. X. *Mater. Chem. Phys.* **2012**, *133*, 480–486.
(10) Liu, H.; Liu, Y.; Zhu, D. *J. Mater. Chem.* **2011**, *21*, 3335–3345.
(11) Xu, Y.; Shi, G. *J. Mater. Chem.* **2011**, *21*, 3311–3323.
(12) Dreyer, D. R.; Murali, S.; Zhu, Y.; Ruoff, R. S.; Bielawski, C. W. *J. Mater. Chem.* **2011**, *21*, 3443–3447.
(13) Grayfer, E. D.; Nazarov, A. S.; Makotchenko, V. G.; Kim, S.-J.; Fedorov, V. E. *J. Mater. Chem.* **2011**, *21*, 3410–3414.
(14) Nursanto, E. B.; Nugroho, A.; Hong, S. A.; Kim, S. J.; Chung, K. Y.; Kim, J. *Green. Chem.* **2011**, *13*, 2714–2718.
(15) Lei, Y. D.; Tang, Z. H.; Liao, R. J.; Guo, B. C. *Green. Chem.* **2011**, *13*, 1655–1658.
(16) Yang, J.; Deng, S. Y.; Lei, J. P.; Ju, H. X.; Gunasekaran, S. *Biosens. Bioelectron.* **2011**, *29*, 159–166.
(17) Xu, Y.; Sheng, K.; Li, C.; Shi, G. *ACS Nano* **2010**, *4*, 4324–4330.
(18) Zhang, S. P.; Xiong, P.; Yang, X. J.; Wang, X. *Nanoscale* **2011**, *3*, 2169–2174.
(19) Lee, J. Y.; In, I. *Chem. Lett.* **2011**, *40*, 567–569.
(20) Liu, J. B.; Fu, S. H.; Yuan, B.; Li, Y. L.; Deng, Z. X. *J. Am. Chem. Soc.* **2010**, *132*, 7279–7281.
(21) Chen, M. L.; Liu, J. W.; Hu, B.; Wang, J. H. *Analyst* **2011**, *136*, 4277–4283.
(22) Lu, F.; Zhang, S. H.; Gao, H. J.; Jia, H.; Zheng, L. Q. *ACS Appl. Mater. Interfaces* **2012**, *4*, 3278–3284.
(23) Nepal, D.; Geckeler, K. E. *Small* **2006**, *2*, 406–412.
(24) Yang, F.; Liu, Y. Q.; Gao, L. A.; Sun, J. *J. Phys. Chem. C* **2010**, *114*, 22085–22091.
(25) Lin, T. H.; Lin, C. W.; Liu, H. H.; Sheu, J. T.; Hung, W. H. *Chem. Commun.* **2011**, *47*, 2044–2046.
(26) Selvakannan, P. R.; Swami, A.; Srisathiyanarayanan, D.; Shirude, P. S.; Pasricha, R.; Mandale, A. B.; Sastry, M. *Langmuir* **2004**, *20*, 7825–7836.
(27) Xie, J. P.; Lee, J. Y.; Wang, D. I. C.; Ting, Y. P. *ACS Nano* **2007**, *1*, 429–439.
(28) Bose, S.; Kuila, T.; Mishra, A. K.; Kim, N. H.; Lee, J. H. *J. Mater. Chem.* **2012**, *22*, 9696–9703.

(29) Zhou, C. Z.; Confalonieri, F.; Jacquet, M.; Perasso, R.; Li, Z. G.; Janin, J. *Proteins* **2001**, *44*, 119−122.
(30) Ha, S. W.; Gracz, H. S.; Tonelli, A. E.; Hudson, S. M. *Biomacromolecules* **2005**, *6*, 2563−2569.
(31) Murphy, C. J.; San, T. K.; Gole, A. M.; Orendorff, C. J.; Gao, J. X.; Gou, L.; Hunyadi, S. E.; Li, T. *J. Phys. Chem. B* **2005**, *109*, 13857−13870.
(32) Willets, K. A.; Van Duyne, R. P. In *Annu. Rev. Phys. Chem.* **2007**; Vol. *58*, p 267-297.
(33) Murray, C. B.; Kagan, C. R.; Bawendi, M. G. *Annu. Rev. Mater. Sci.* **2000**, *30*, 545−610.
(34) Skrabalak, S. E.; Chen, J. Y.; Sun, Y. G.; Lu, X. M.; Au, L.; Cobley, C. M.; Xia, Y. N. *Acc. Chem. Res.* **2008**, *41*, 1587−1595.
(35) Au, L.; Zheng, D. S.; Zhou, F.; Li, Z. Y.; Li, X. D.; Xia, Y. N. *ACS Nano* **2008**, *2*, 1645−1652.
(36) Tognalli, N. G.; Fainstein, A.; Calvo, E. J.; Abdelsalarn, M.; Bartlett, P. N. *J. Phys. Chem. C* **2012**, *116*, 3414−3420.
(37) Raveendran, P.; Fu, J.; Wallen, S. L. *Green. Chem.* **2006**, *8*, 34−38.
(38) Shao, Y.; Jin, Y. D.; Dong, S. J. *Chem. Commun.* **2004**, 1104−1105.
(39) Wirtz, M.; Martin, C. R. *Adv. Mater.* **2003**, *15*, 455−458.
(40) Sau, T. K.; Murphy, C. J. *J. Am. Chem. Soc.* **2004**, *126*, 8648−8649.
(41) Au, L.; Chen, Y. C.; Zhou, F.; Camargo, P. H. C.; Lim, B.; Li, Z. Y.; Ginger, D. S.; Xia, Y. N. *Nano. Res.* **2008**, *1*, 441−449.
(42) Tang, X. L.; Jiang, P.; Ge, G. L.; Tsuji, M.; Xie, S. S.; Guo, Y. J. *Langmuir* **2008**, *24*, 1763−1768.
(43) Feng, J. J.; Li, A. Q.; Lei, Z.; Wang, A. J. *ACS Appl. Mater. Interfaces* **2012**, *4*, 2570−2576.
(44) Jasuja, K.; Berry, V. *ACS Nano* **2009**, *3*, 2358−2366.
(45) Xie, J. P.; Zhang, Q. B.; Lee, J. Y.; Wang, D. I. C. *ACS Nano* **2008**, *2*, 2473−2480.
(46) Wang, L.; Liu, C. H.; Nemoto, Y.; Fukata, N.; Wu, K. C. W.; Yamauchi, Y. *RSC Adv.* **2012**, *2*, 4608−4611.
(47) Dong, X. C.; Huang, W.; Chen, P. *Nanoscale. Res. Lett.*. **2011**, 6.
(48) Shen, J. F.; Yan, B.; Shi, M.; Ma, H. W.; Li, N.; Ye, M. X. *J. Mater. Chem.* **2011**, *21*, 3415−3421.
(49) Shen, J. F.; Shi, M.; Yan, B.; Ma, H. W.; Li, N.; Ye, M. X. *J. Mater. Chem.* **2011**, *21*, 7795−7801.
(50) Huang, J.; Zhang, L. M.; Chen, B. A.; Ji, N.; Chen, F. H.; Zhang, Y.; Zhang, Z. J. *Nanoscale* **2010**, *2*, 2733−2738.
(51) Liang, Y. Y.; Wang, H. L.; Zhou, J. G.; Li, Y. G.; Wang, J.; Regier, T.; Dai, H. J. *J. Am. Chem. Soc.* **2012**, *134*, 3517−3523.
(52) Kou, R.; Shao, Y. Y.; Mei, D. H.; Nie, Z. M.; Wang, D. H.; Wang, C. M.; Viswanathan, V. V.; Park, S.; Aksay, I. A.; Lin, Y. H.; Wang, Y.; Liu, J. *J. Am. Chem. Soc.* **2011**, *133*, 2541−2547.
(53) Wu, Z. S.; Yang, S. B.; Sun, Y.; Parvez, K.; Feng, X. L.; Mullen, K. *J. Am. Chem. Soc.* **2012**, *134*, 9082−9085.
(54) Yang, Z.; Yao, Z.; Li, G. F.; Fang, G. Y.; Nie, H. G.; Liu, Z.; Zhou, X. M.; Chen, X.; Huang, S. M. *ACS Nano* **2012**, *6*, 205−211.
(55) Li, Y.; Zhao, Y.; Cheng, H. H.; Hu, Y.; Shi, G. Q.; Dai, L. M.; Qu, L. T. *J. Am. Chem. Soc.* **2012**, *134*, 15−18.
(56) Qu, L. T.; Liu, Y.; Baek, J. B.; Dai, L. M. *ACS Nano* **2010**, *4*, 1321−1326.
(57) Yang, Y. H.; Shao, Z. Z.; Chen, X.; Zhou, P. *Biomacromolecules* **2004**, *5*, 773−779.
(58) Hummers, W. S.; Offeman, R. E. *J. Am. Chem. Soc.* **1958**, *80*, 1339−1339.
(59) Li, D.; Muller, M. B.; Gilje, S.; Kaner, R. B.; Wallace, G. G. *Nat. Nanotechnol.* **2008**, *3*, 101−105.
(60) Novoselov, K. S.; Geim, A. K.; Morozov, S. V.; Jiang, D.; Zhang, Y.; Dubonos, S. V.; Grigorieva, I. V.; Firsov, A. A. *Science* **2004**, *306*, 666−669.
(61) Lu, G.; Li, C.; Shi, G. *Chem. Mater.* **2007**, *19*, 3433.
(62) Song, H. M.; Anjum, D. H.; Khashab, N. M. *RSC Adv.* **2012**, *2*, 3621.
(63) Quaresma, P.; Soares, L.; Contar, L.; Miranda, A.; Osorio, I.; Carvalho, P. A.; Franco, R.; Pereira, E. *Green. Chem.* **2009**, *11*, 1889.
(64) Zhang, B.; Zhao, B. T.; Huang, S. H.; Zhang, R. Y.; Xu, P.; Wang, H. L. *Crystengcomm* **2012**, *14*, 1542.
(65) Choi, B. G.; Yang, M. H.; Park, T. J.; Huh, Y. S.; Lee, S. Y.; Hong, W. H.; Park, H. *Nanoscale* **2011**, *3*, 3208.
(66) Jahan, M.; Bao, Q. L.; Loh, K. P. *J. Am. Chem. Soc.* **2012**, *134*, 6707.
(67) Li, Z. Q.; Li, W. Y.; Camargo, P. H. C.; Xia, Y. N. *Angew. Chem., Int. Ed.* **2008**, *47*, 9653.
(68) Gong, K. P.; Du, F.; Xia, Z. H.; Durstock, M.; Dai, L. M. *Science* **2009**, *323*, 760.
(69) Liu, R. L.; Wu, D. Q.; Feng, X. L.; Mullen, K. *Angew. Chem., Int. Ed.* **2010**, *49*, 2565.